Materials Research Express

PAPER

RECEIVED
2 March 2017

REVISED
2 May 2017

ACCEPTED FOR PUBLICATION
31 May 2017

PUBLISHED
5 July 2017

Optical properties of nanocrystallite films of α-Fe_2O_3 and α-$Fe_{2-x}Cr_xO_3$ ($0.0 \leqslant x \leqslant 0.9$) deposited on glass substrates

Ajay Kumar and Kamlesh Yadav

Centre for Physical Sciences, Central University of Punjab, Bathinda 151001, India

E-mail: kamlesh.yadav001@gmail.com **and** kamlesh_yadav@cup.ac.in

Keywords: iron oxide, optical properties, spray pyrolysis, films

Abstract

α-Fe_2O_3 films are deposited on fluorine-doped tin oxide (FTO) and indium-doped tin oxide (ITO) substrates for 1, 4 and 6 min using a spray pyrolysis technique. We also deposited α-$Fe_{2-x}Cr_xO_3$ ($x = 0.0, 0.1, 0.2, 0.3, 0.4, 0.7$ and 0.9) films on the FTO substrate for a deposition time of 35 s. The structural and optical properties of these films were then studied. The x-ray diffraction (XRD) patterns show that all the films are crystalline in nature with a hexagonal crystal structure. The average grain size and unit cell volume were calculated using XRD data. It is found that the average grain size and unit cell volume increase with an increasing film thickness and Cr-doping concentration. The value of strain decreases with an increasing film thickness and Cr-doping content. It is also found that films with the same deposition time on the ITO substrate are more crystalline than on the FTO substrate. Furthermore, the average grain size is obtained from field emission scanning electron microscopy (FESEM) images. FESEM analysis confirms that the average grain size increases with the film thickness and Cr-doping concentration. The optical absorption spectra of the films show that the absorbance increases with an increasing deposition time and Cr concentration. The energy band gap (E_g) of all the films has been calculated using Tauc's relation. A narrowing of the band gap was observed with an increase in film thickness and Cr-doping content. The reduction of the band gap with the increase in film thickness of the films deposited on the ITO substrate is larger than for the film deposited on the FTO substrate. The refractive index is also obtained from the absorption spectra of the films using the Moss relation: $n = \sqrt[4]{(k/E_g)}$, where $k = 108$ eV. The refractive index decreases with an increase in the optical band gap. The band gaps of the films are also calculated from the FTIR spectra. This is in good agreement with the UV data. The correlation between the structural and optical properties of the deposited films has been discussed.

1. Introduction

Thin film deposition has been the subject of intensive study for almost a century. A variety of different techniques can be used to deposit the films, including chemical solution routes like sol–gel [1], spin coating, dip coating [2] and spray pyrolysis [3]. The formation of a thin film takes place via nucleation and growth processes on the surface of the substrate. The thin film is usually strained up to a certain critical film thickness, beyond which misfit dislocations are introduced [4]. Stress is generated in the film due to the lattice mismatch between the substrate and deposited material, which subsequently affects the properties of the thin film. The thin film properties are also affected significantly by the formation of crystalline defects, hillocks and whiskers during the deposition of the film [5, 6].

Iron oxide thin film has extensive and significant applications in semiconductor devices, magneto-optic memories, audio–video systems, computer chips and in memory storage devices [7]. Iron oxide exists in three phases: α-Fe_2O_3, β-Fe_2O_3, γ-Fe_2O_3, and the various phases of iron oxide can be changed into other forms by varying the temperature and oxygen pressure, etc. Bulk α-Fe_2O_3 is useful in water splitting processes to produce hydrogen fuel. It is also very useful in photocatalysis (band gap 2.2 eV) and has high photostability. However, in spite

of these qualities it suffers from a low hole diffusion length, a short exciton lifetime (~10 ps), poor minority charge carrier mobility, and limited light penetration depth. The maximum reported efficiency of the water splitting of α-Fe_2O_3 is 12.9% [8]. It has been reported by many researchers that the doping of different metal cations (Mg^{2+}, Ca^{2+}, Ti^{4+}, and Zn^{2+} etc) in iron oxide decreases the formation of defects and enhances the photoconversion efficiency [9–13]. The nano-scaling of bulk α-Fe_2O_3 also increases the photoconversion efficiency. The α-Fe_2O_3 (hematite) has a corundum rhombohedral/hexagonal-type structure [13]. It has been reported by many researchers that the film thickness affects the optical and structural properties of the α-Fe_2O_3 films. It is also reported that the energy gap (E_g) of the films decreases with increasing film thickness [14]. The doping of transition elements such as Cr, Zn, Ni, Mg and Pt enhances the photoconversion efficiency of nanocrystalline thin films of α-Fe_2O_3 [15–18]. The band gap decreases and absorbance increases with increasing Cr-doping in α-Fe_2O_3 film [8, 19–21]. There are various techniques used for the thin film deposition of α-Fe_2O_3 such as electrodeposition [19], molecular beam epitaxy (MBE) [21], microemulsion-based methods [22], spray pyrolysis [10], hydrothermal and sol–gel [23].

In the present paper, we have studied the effect of thickness, the nature of the substrates, and the Cr-doping concentration on the structural and optical properties of α-$Fe_{2-x}Cr_xO_3$ ($x = 0.0, 0.1, 0.2, 0.3, 0.4, 0.7$ and 0.9) thin films deposited on fluorine-doped tin oxide (FTO) and indium-doped tin oxide (ITO) glass substrates.

2. Experimental procedure

The α-Fe_2O_3 thin films were deposited onto the FTO and ITO glass substrates by the spray pyrolysis method (Holmarc spray pyrolysis set-up). 0.3 M solution of ferric chloride ($FeCl_3$) was prepared in distilled water. The prepared solution was continually stirred with a magnetic stirrer for 1 h 30 min at 50 °C. A few drops of methanol (15–18) were added to the solution for proper evaporation of the solvent during the deposition process. The films were deposited under the following conditions: (i) substrate temperature: 450 °C, (ii) distance between the nozzle and substrate: 22 cm, (iii) pressure of carrier gas: 0.6 bar, (iv) liquid flow rate: 0.5 ml min^{-1}. We deposited films on the heated ITO and FTO substrates for 1, 4 and 6 min. The deposited films were heated at 300 °C for 5 h in a vacuum. Further, the films were annealed at 650 °C for 1 h 30 min.

Polycrystalline films with the composition α-$Fe_{2-x}Cr_xO_3$ ($x = 0, 0.1, 0.2, 0.3, 0.4, 0.7$ and 0.9) were also prepared using this technique. 0.3 M ferric nitrate ($Fe_2(NO_3)_3.9H_2O$) and 0.3 M chromium nitrate ($Cr_2(NO_3).9H_2O$) were mixed. The solution was placed under magnetic stirring at 50 °C for 1 h 30 min. All other conditions were kept the same as in the deposition of the undoped films. The structural properties of the prepared films were characterized using x-ray diffraction (PAN-analytical XPERT-PRO). The surface morphology and elemental composition of the thin films were studied using field emission scanning electron microscopy (FESEM) and energy dispersive x-ray spectroscopy (EDX) (Carl Zeiss, Merlin Compact) respectively. The absorbance spectra of the films were recorded in the wavelength range 200–800 nm using a UV-2450 spectrophotometer (Shimadzu). Ultraviolet–visible Fourier transform infrared spectroscopy (UV–Vis-FTIR) spectra were recorded in the wavenumber range 400–4000 cm^{-1} using a Brucker Tensor-27 Spectrophotometer.

3. Results and discussions

3.1. X-ray diffraction (XRD) analysis

Figure 1(a) shows the XRD patterns of α-Fe_2O_3 films that are deposited for 1 and 6 min on FTO and ITO substrates. Figure 1(b) shows the XRD patterns of α-$Fe_{2-x}Cr_xO_3$ films with $x = 0.4$ and 0.7, which were deposited on FTO substrates for a deposition time of 35 s. The sharp peaks indexed at (1 0 4), (1 1 0), (1 1 3) and (1 1 6) clearly indicate single phase α-Fe_2O_3 with a hexagonal structure as well as the well crystalline nature of the film [24–26]. This is due to the films being annealed at 650 °C for 1 h 30 min, resulting in single-phase crystalline films of α-Fe_2O_3; the color of the film also changed from yellow to red after annealing. This confirms the successful conversion of FeOOH to α-Fe_2O_3. Fe atoms are oxidized to their +3 oxidation state at higher temperatures, which leads to the formation of a pure α-Fe_2O_3 phase [27, 28]. The diffraction peak intensities are enhanced as the deposition time increases, which is attributed to the observed increase in the film thickness. Furthermore, no additional peaks corresponding to any secondary phases were observed in the XRD patterns. Moreover, the intensity of the FTO substrate peaks in α-$Fe_{2-x}Cr_xO_3$ films with Cr concentrations $x = 0.4$ and 0.7 are suppressed (see figure 1(b)). This generally occurs in solvothermal methods as reported by Mu *et al* [29]. It is reported in the literature that the full removal of hydroxyls from α-Fe_2O_3 generally requires annealing over 800 °C [30]. The suppression of FTO peaks in the Cr-doped films deposited on the FTO substrate clearly indicates the presence of water in these samples, as reported by others [30]. The suppression of FTO peaks in the Cr-doped samples also suggests that the Cr^{3+} dopant strongly interacts with the hydroxyl groups present in the water. However, all the ITO and FTO peaks are indexed in the case of undoped films deposited on ITO and FTO substrates, indicating the maximum removal of water, although the intensity of the ITO peaks is found to be more than the FTO peaks, signifying more removal of water in the case of films deposited on the ITO substrate. This also confirms the small amount of amorphization

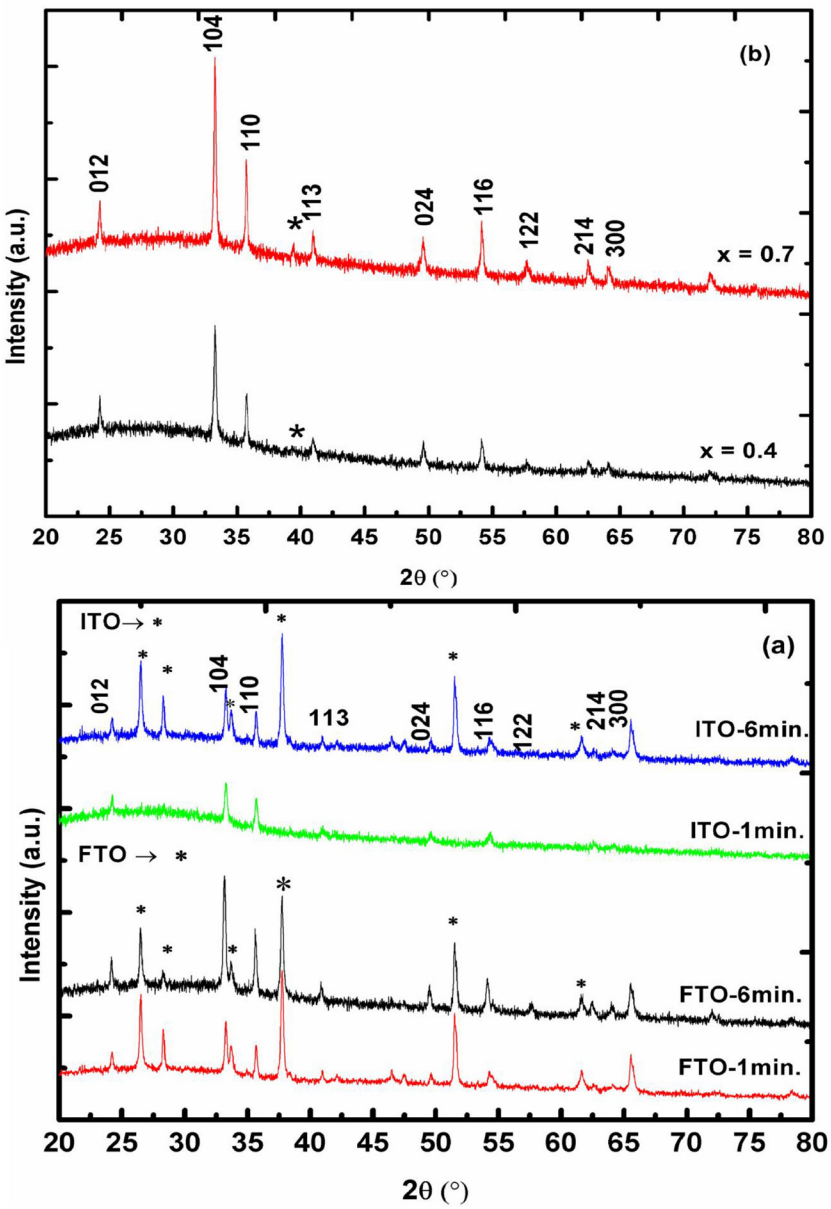

Figure 1. (a) X-ray diffraction patterns of α-Fe_2O_3 films on the FTO substrate for times of 1 min and 6 min; (b) x-ray diffraction patterns of doped α-$Fe_{2-x}Cr_xO_3$ films for $x = 0.4$ and $x = 0.7$.

attributed to the film deposited on the FTO substrate. The lattice parameters are calculated by using the equation, $\frac{1}{d^2} = \frac{4}{3a^2}(h^2 + k^2 + hk) + \frac{l^2}{c^2}$; here, $(h\,k\,l)$ represent the Miller indices and d represents the inter-planer spacing between the crystal planes [31]. The values of the lattice parameters for all the samples are given in table 1, and they agree well with the published values [17, 19, 25]. The unit cell volume of the films is calculated using the formula volume $(V) = 0.866 \times a^2 \times c$, where a and c are the crystallographic axis [32]. The unit cell volumes of the films on the FTO and ITO substrates with a deposition time of 6 min are found to be larger than the films with a deposition time of 1 min (see table 1). This result can be explained on the basis of variation in the strain of the film with the deposition time. Therefore, the values of strain are calculated using $\varepsilon = \frac{\beta \cos\theta}{4}$; here, β is the full width at half maxima and θ is the diffraction angle [33–38] (see table 2). It is also observed that the film with a deposition time of 1 min has a larger strain than the film that is deposited for 6 min (see table 2) [33]. The reduction in strain with the increase in film thickness is well reported [34–36]. This leads to an increase in the unit cell volume for the films deposited for 6 min over the films deposited for 1 min (see table 2) [34, 35]. Besides this, the decrease in strain with the increase in deposition time is larger for the films that are deposited on the ITO substrate than the films on the FTO substrates. The reaction of Fe^{3+} with the hydroxyl ions present in the films deposited on the FTO substrate hinders the growth of the film, indicating less reduction in strain in the case of films deposited on FTO substrates [39]. Moreover, the reaction of Fe^{3+} with OH^- leads to more values of strain for the films on the FTO substrates than the films on the ITO substrates for an equal deposition time (see table 2). All these results indicate that the

Table 1. Structural parameters of α-Fe_2O_3 and Cr-doped α-Fe_2O_3 films calculated from x-ray diffraction pattern.

S. no.	Sample	a (nm)	c (nm)	Average grain size (nm)	Volume (nm^3)
1.	FTO-1 min	0.504 18	1.363 35	62	0.300 12
2.	FTO-6 min	0.504 19	1.374 83	72	0.302 66
3.	ITO-1 min	0.503 43	1.371 34	89	0.300 98
4.	ITO-6 min	0.503 39	1.371 98	111	0.301 07
5.	$x = 0.4$, FTO-35 s	0.503 26	1.367 56	48	0.299 95
6.	$x = 0.7$, FTO-35 s	0.503 49	1.369 86	57	0.300 72

Table 2. The values of c/a ratio, bond length (l) and micro-strain (ε) of α-Fe_2O_3 and Cr-doped α-Fe_2O_3 films.

S. no.	Samples	c/a ratio	Bond length, l (Å)	Micro-strain (ε) 10^{-3}
1.	FTO-1 min	2.7040	4.029 76	0.5023
2.	FTO-6 min	2.7268	4.053 41	0.4342
3.	ITO-1 min	2.7246	4.044 41	0.4703
4.	ITO-6 min	2.7254	4.045 83	0.3492
5.	$x = 0.4$	2.7174	4.036 23	0.7367
6.	$x = 0.7$	2.7207	4.04 151	0.6297

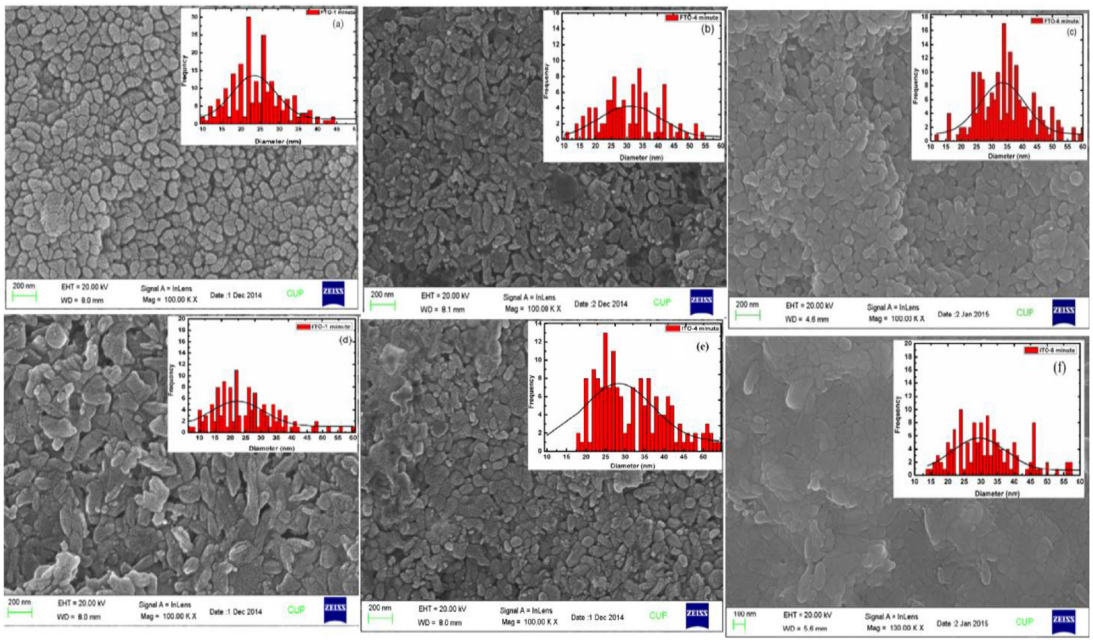

Figure 2. (a)–(c) FE-SEM images of undoped α-Fe_2O_3 films on the FTO substrate for 1 min, 4 min and 6 min; (d)–(f) FE-SEM images of α-Fe_2O_3 films on the ITO substrate for 1 min, 4 min and 6 min. Insets show the histogram plotted between the grain size (nm) and the frequency of occurrence of the grains in the FESEM micrograph.

Table 3. The values of the average grain size of α-Fe_2O_3 film on the FTO and ITO substrates calculated from FESEM micrographs.

S. no.	Deposition time	Average grain size (nm)
1.	FTO-1 min	24
2.	FTO-4 min	31
3.	FTO-6 min	34
4.	ITO-1 min	22
5.	ITO-4 min	28
6.	ITO-6 min	29

Table 4. The values of the average grain size of α-$Fe_{2-x}Cr_xO_3$ (where $x = 0.0, 0.1, 0.2, 0.3, 0.4, 0.7$ and 0.9) films on the FTO substrate calculated from FESEM micrographs.

S. no.	Cr content	Average grain size (nm)
1.	0	20
2.	0.1	22
3.	0.2	23
4.	0.3	25
5.	0.4	26
6.	0.7	30
7.	0.9	36

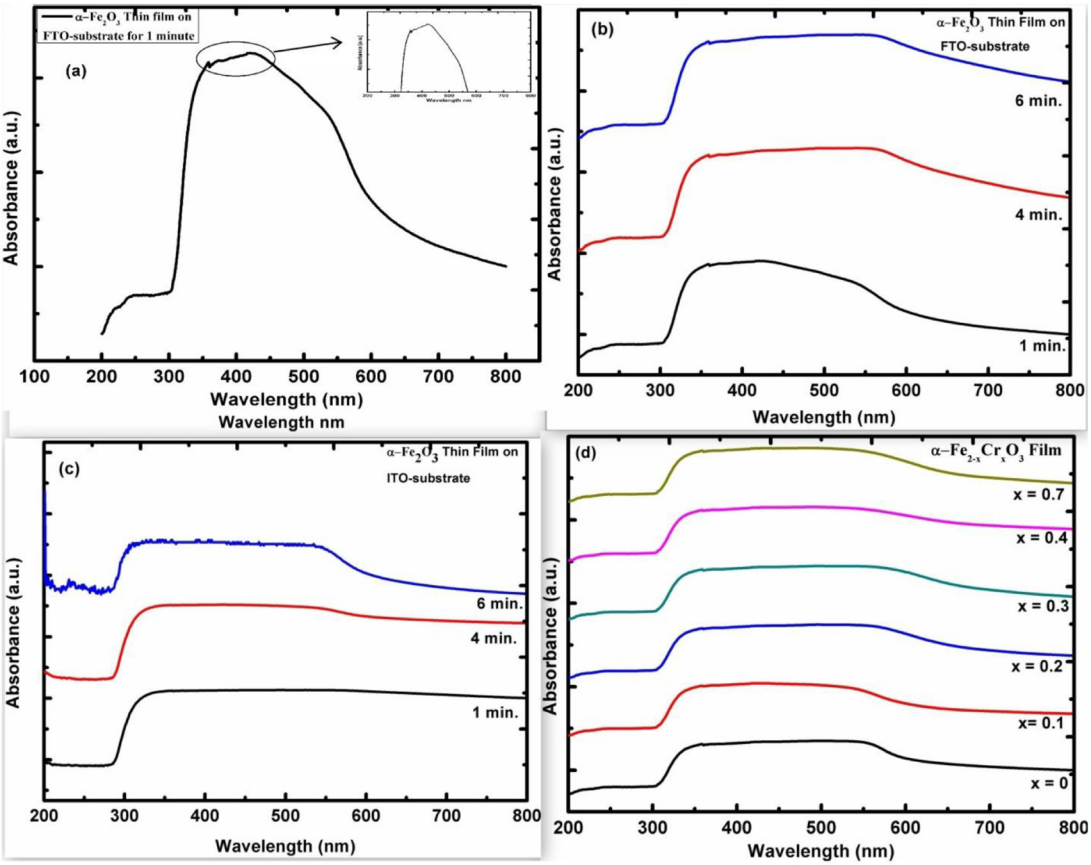

Figure 3. UV–visible spectra of α-Fe_2O_3 films (a) for 1 min on the FTO substrate (inset shows the band edges), (b) for 1 min, 4 min and 6 min on the FTO substrate, (c) for 1 min, 4 min and 6 min on the ITO substrate, (d) α-$Fe_{2-x}Cr_xO_3$ (where $x = 0, 0.1, 0.2, 0.3, 0.4, 0.7$ and 0.9) films on the FTO substrate.

ITO substrate is more suitable for the deposition of α-Fe_2O_3 films at a low annealing temperature, indicating that it is a suitable candidate for technological applications in optoelectronic devices. It is also found that the unit cell volume increases with an increase in the Cr-doping. However, this result cannot be explained on the basis of the ionic radii mismatch, since the ionic radii of Fe^{3+} (0.0645 nm) is more than the Cr^{3+} (0.064 nm) [40]. Therefore, this suggests that the expansion of unit cell volume with an increase in the Cr-doping content is due to an increase in the interaction between the Cr^{3+} and OH^- groups. Hence, the amount of water attached to the Cr^{3+} during spray pyrolysis increases with an increase in Cr-doping content, which leads to an expansion of the unit cell volume. In addition to this, an increase in the intensity of the diffraction peaks ((1 1 0), (1 1 3), etc) is observed with an increase in the thickness of the film and doping content. This indicates the increase in the crystalline nature of the α-Fe_2O_3 films with the thickness of the film and doping content. The increase in peak intensity with Cr-doping also confirms the enhancement of the relaxation of the residual stress in the Cr-doped films over the undoped films [21]. It may also be noted that the XRD patterns of the Cr-doped films have fewer XRD peaks, unlike that of the undoped films. This confirms that the undoped films have a lower crystal symmetry [41]. We have also

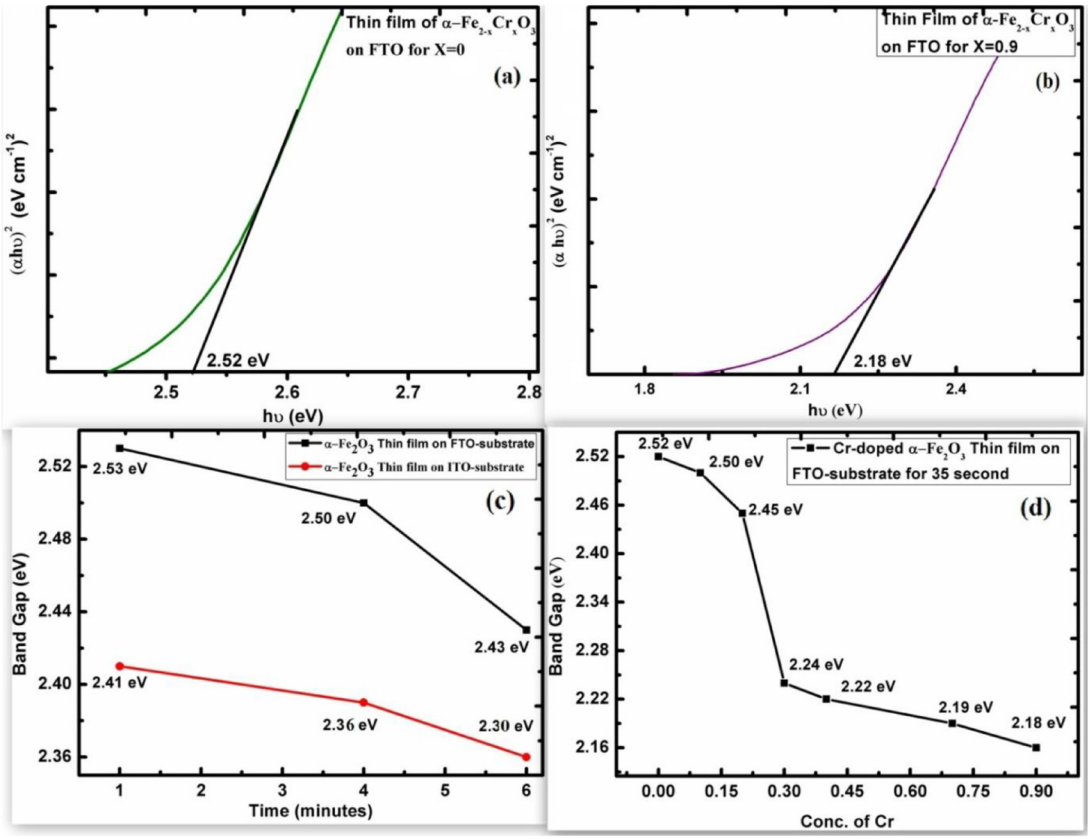

Figure 4. Calculation of the direct band gap of α-$Fe_{2-x}Cr_xO_3$ films (a) for $x = 0.0$ on the FTO substrate, (b) for $x = 0.9$ on the FTO substrate, (c) the direct band gap variation with deposition time on the FTO (black) and the ITO (red) substrate, (d) the variation of the direct band gap with the Cr concentration for films on the FTO substrate.

calculated the *c*/*a* ratio and bond length (l) of the films. The bond length of the films is calculated using the equation $(l) = \sqrt{\left(\frac{a^2}{3} + \left(\frac{1}{2} - u\right)^2 c^2\right)}$, where $u = \frac{a^2}{3c^2} + 0.25$ [36, 42]. An increase in the bond length with an increase in film thickness and Cr-doping is observed. This is due to the increase in the unit cell volume [21, 43, 44]. The *c*/*a* ratio of the films increases with the increasing film thickness and doping content [41]. This also confirms the stress relaxation of the films with the increase in film thickness and doping. The average values of the grain sizes of the films are calculated using the Debye–Scherrer equation, $D = \frac{0.9\lambda}{\beta \cos\theta}$, where $\lambda = 1.5406$ Å, and β is the full width at half maxima of the diffracted peaks [31], as given in table 1. The grain size of the films on the FTO and ITO substrates increases with an increase in the film deposition time. It also increases with the increase in Cr-doping content, as given in table 1. The increase in the grain size with the increase in the deposition time and Cr concentration is in good agreement with the reported literature [19, 21, 44, 45]. The increase in the deposition time causes an increase in solute particles over the substrate. This results in the enhancement of the electrostatic interaction of the solute particles. Solute particle gathering takes place at the substrate, enhancing the grain size [46]. In the case of Cr-doped thin films, Cr-doping leads to an increase in interaction between the Cr^{3+} and hydroxyl group, resulting in a decrease in strain energy and hence an increase in grain size [47, 48]. Moreover, the value of the average grain size of the films on the ITO substrate is larger than the films on the FTO substrate when compared at the same deposition time. Also, the decrease in the average grain size with increasing deposition time is larger in case of the films on the ITO substrates. These results indicate that the film's crystallinity increases with an increasing deposition time. Moreover, all these results indicate that the films deposited on the ITO substrate are more crystalline than the films on the FTO substrate [49].

3.2. FESEM analysis

FESEM images of the α-Fe_2O_3 films on FTO, and ITO substrates are shown in figures 2(a)–(f) respectively. The FESEM images show prolonged grains for all the films. The average values of grain size for all the samples are calculated by the Gaussian curve fitting of the histograms, which is plotted between the grain size (nm) and the frequency of occurrence of the grains in the FESEM micrograph (see the inset of figure 2). The grain size increases with the increasing film deposition time and Cr-doping concentration (see tables 3 and 4) [26, 42, 47, 48, 50, 51]. This result is in good agreement with those obtained by XRD. We have also characterized all the samples with the

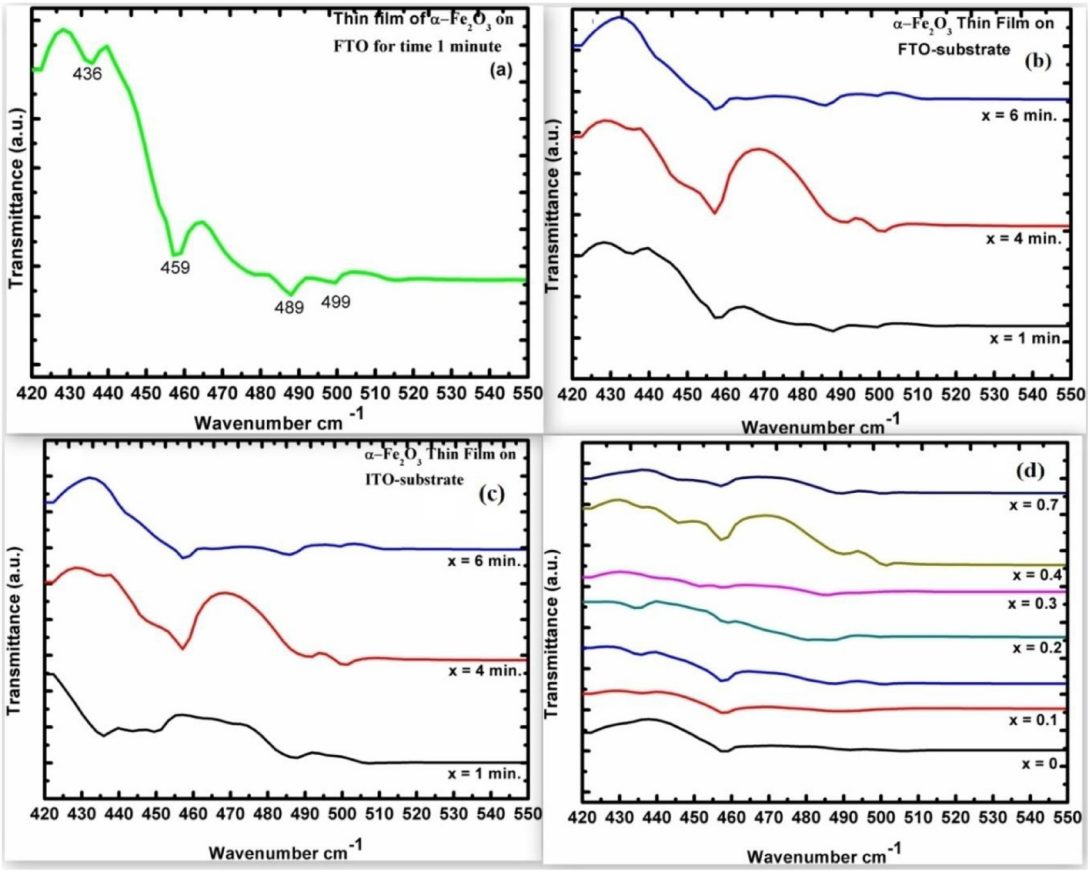

Figure 5. (a) FTIR spectra of α-Fe_2O_3 film on the FTO substrate for 1 min, (b) FTIR spectra of α-Fe_2O_3 film on the FTO substrate for 1 min, 4 min and 6 min, (c) FTIR spectra of α-Fe_2O_3 on the ITO substrate for 1 min, 4 min and 6 min, (d) FTIR spectra of α-$Fe_{2-x}Cr_xO_3$ (where $x = 0.0, 0.1, 0.2, 0.3, 0.4, 0.5, 0.7$ and 0.9) films that are deposited for 35 s on the FTO substrate.

EDS. It is found that no impurity elements are present, and elemental compositions of the samples are confirmed within the experimental error.

3.3. UV–visible spectrum analysis

UV–visible optical absorption spectra of α-Fe_2O_3 films on the FTO and ITO substrates are shown in figures 3(a)–(c), and for the Cr-doped samples in figure 3(d). Two absorption edges are observed between 300–450 nm and 450–550 nm for the films on the FTO substrate with the deposition time of 1 min (see figure 3(a) and its inset). These bands arise due to the $^6A_1 - {}^4T_2$ ligand field transitions and the pair of excitation transition processes $^6A_1 + {}^6A_1 \rightarrow {}^4T_2\,(^4G) + {}^4T_2(^4G)$ of two adjacent Fe^{3+} centers [35, 46–48]. These absorption edges completely disappear with the increase in the wavelength. Further, a decrease in the absorbance is observed with an increasing wavelength. Finally, this variation becomes linear in the red region (figures 3(b)–(d)). This linear region is due to the increase in charge transfer transitions in the higher wavelength region [52, 53]. The intensity of the absorption peak increases with the increasing deposition time and Cr content, as reported by Nematollahi *et al* [54]. The energy band gap values for different absorption peaks are calculated from Tauc's relation,

$$\alpha h\upsilon = A(h\upsilon - E_g)^n$$

$$\text{where } A = \left[\frac{e^2}{nch^2 m_e^*}\right]\sqrt[3]{(2m_r)}$$

and m_e^* and m_r represent the effective mass and reduced mass of the charge carriers, α is the absorption coefficient, and E_g is the optical energy gap value (eV), which depends on the crystalline structure. Here, h is the plank's constant with a value $= 6.626 \times 10^{-34}$ J s^{-1} and υ is the frequency of the irradiated light. A is a constant that depends on the type of material used [51]. The value of 'n' depends on the type of transitions, and is 1/2 or 3/2 for direct transitions [55]. The energy gap value is calculated using the plot $(\alpha h\upsilon)^{1/n}$ versus E_g by extrapolating the linear part, giving a band energy value at $\alpha = 0$ (see figures 4(a) and (b)). The O^{2-} 2p to Fe^{3+} (charge-transfer) transitions are responsible for the direct energy gap values [34, 56]. The band gap of the films decreases with an increase in film thickness, as shown in figure 4(c) [34, 57]. This result is due to the increase in grain size, which also

Table 5. Calculated wave numbers of Fe-O transverse vibrational mode from FTIR analysis of α-Fe_2O_3 films on FTO and ITO substrates.

S. no.	α-Fe_2O_3 film	Wave number (cm^{-1})	Mode
1.	FTO-1 min	436, 459, 489, 499	E_u
2.	FTO-4 min	436, 445, 457, 490	E_u
3.	FTO-6 min	438, 458, 493	E_u
4.	ITO-1 min	436, 450, 488	E_u
5.	ITO-4min	458, 491	E_u
6.	ITO-6 min	457, 486	E_u

Table 6. Wavenumbers corresponding to Fe-O transverse vibrational mode from FTIR analysis of α-$Fe_{2-x}Cr_xO_3$ (where $x = 0.0, 0.1, 0.2, 0.3, 0.4, 0.7$ and 0.9) films on FTO substrate.

S. no.	Sample (α-$Fe_{2-x}Cr_xO_3$)	Wave number (cm^{-1})
1.	$x = 0$	457, 490
2.	$x = 0.1$	436, 458, 491
3.	$x = 0.2$	435, 459, 488, 501
4.	$x = 0.3$	435, 459, 488
5.	x =0.4	450, 459, 488
6.	$x = 0.7$	445, 458, 491, 501
7.	$x = 0.9$	458, 490, 502

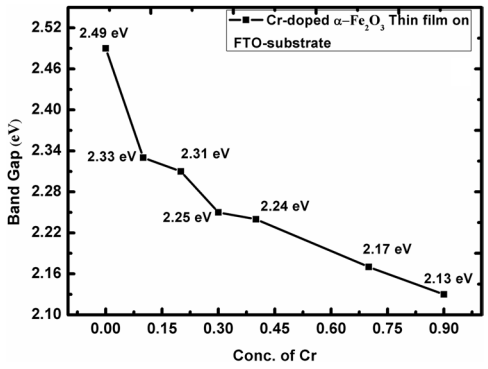

Figure 6. Variation of the direct band gap of α-$Fe_{2-x}Cr_xO_3$ (where $x = 0.0, 0.1, 0.2, 0.3, 0.4, 0.5, 0.7$ and 0.9) films with the Cr-doping concentration on the FTO substrate.

leads to a change in the grain boundary barrier height, and also stress relaxation in the film with the increase in film thickness [57, 58]. The value of the energy band gap is less in the case of films deposited on the ITO substrate than the FTO substrate. This is due to the greater conductivity of the ITO substrate than the FTO substrate [59]. The band gap of Fe_2O_3 is found to be 2.51 eV, which is higher than the reported value of 2.1 eV in Fe_2O_3 thin films [60]. This further indicates that the Fe^{3+} exists in a low spin state, which results in an increase in the band gap of Fe_2O_3. The band gap decreases with increasing Cr content (see figure 4(d)). The decrease in band gap is nearly 13.5% as the concentration (x) of Cr is increased from 0 to 0.9 (figure 4(d)). This may be ascribed to an increase in impurities as well as structural disorders with the increase in Cr-doping. The decrease in band gap with the increase in Cr content is also due to partial hybridization between the Cr t_{2g} − Fe t^*_{2g} 3d orbital and the decrease in the residual in-plane compressive strain, as reported by Mashiko *et al* and others [18, 26, 60, 61]. The sharp decrease in band gap arises with the increase in Cr concentration up to $x = 0.3$. Moreover, the decrease in band gap becomes almost linear above $x = 0.3$ (see figure 4(d) [21, 26].

3.4. Ultraviolet–visible Fourier transform infrared spectroscopy (UV–Vis-FTIR) analysis

The UV–vis FTIR spectra of α-Fe_2O_3 films on FTO and ITO substrates and Cr-doped α-Fe_2O_3 films on FTO substrate are shown in figures 5(a)–(d). All the peaks in the UV–Vis-FTIR spectra are indexed with the Fe-O functional groups (see figure 5(a)). This confirms the presence of the α-Fe_2O_3 phase. The values of different wavenumbers at which the minimum transmittance occurs are given in tables 5 and 6 [22, 31, 56]. Moreover, the peak shifts towards higher wavenumbers (cm^{-1}) upon increasing the film thickness and Cr-doping content.

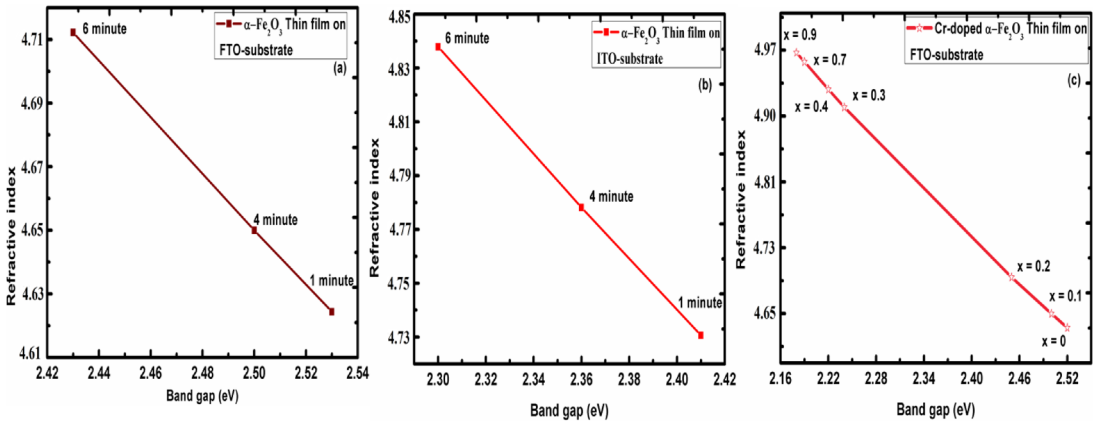

Figure 7. The variation of the refractive index with the band gap for (a) 1 min, 4 min and 6 min on the FTO substrate, (b) 1 min, 4 min and 6 min on the ITO substrate, (c) for the α-$Fe_{2-x}Cr_xO_3$ (where $x = 0.0, 0.1, 0.2, 0.3, 0.4, 0.5, 0.7$ and 0.9) films on the FTO substrate.

This is due to the lattice strain relaxation and the appearance of higher crystal symmetry with increasing film thickness and Cr-doping [62, 63]. The direct band gap of all the films is also calculated from the UV–Vis-FTIR spectra. The variation of the direct band gap with Cr concentration is shown in figure 6 [17, 18]. It is found that the band gap decreases with an increasing Cr-doping content. The results were obtained using the UV–Vis-FTIR spectra, which are consistent with the UV–visible data of the thin films.

We have also calculated the refractive index (n) for α-$Fe_{2-x}Cr_xO_3$ (where $x = 0.0, 0.1, 0.2, 0.3, 0.4, 0.7$ and 0.9) films using the Moss relation $n = \sqrt[4]{\frac{k}{E_g}}$, where k is a constant value of 108 eV and E_g is the band gap [58, 59]. It is observed for all the thin films that the refractive index decreases with an increasing band gap (figures 7(a)–(c)) [57, 58]. This result plays an especially important role in determining the optical properties of the thin films, and helps in the design of optoelectronic devices and solar cells.

4. Conclusions

The optical properties of α-Fe_2O_3 films on FTO and ITO substrates and α-$Fe_{2-x}Cr_xO_3$ ($x = 0.0, 0.1, 0.2, 0.3, 0.4, 0.7$ and 0.9) films on an FTO substrate have been studied. The influence of deposition time on the properties of the films has also been investigated. XRD analysis of the films shows an increase in the average grain size, Fe-O bond length and unit cell volume with an increasing film thickness and Cr-doping content. These results are explained on the basis of the presence of a hydroxyl group in the films deposited on the FTO substrate and the decrease in the strain of the films due to relaxation in compressive stress with the increasing deposition time and Cr-doping. This data reveals that the film on the ITO substrate is more crystalline than the film on the FTO substrate. Hence, it is concluded that ITO is more suitable than FTO for the thin film deposition of α-Fe_2O_3. The increase in grain size of the films with the increase in the film thickness and doping are also confirmed by FESEM micrograph analysis. Furthermore, it is observed that absorbance increases with the increasing deposition time and Cr doping. The band gaps of the films on ITO and FTO substrates decline with the increasing film thickness and Cr-doping concentration. It is also reported that the decline in the band gap on the ITO substrate is larger than on the FTO substrate, which is due to the greater conductivity of the former than the latter. Moreover, it is found that the refractive index of the films decreases with the increasing band gap. These undoped and Cr-doped α-Fe_2O_3 thin films, with a reduced band gap and enhanced absorbance, can be used as electrodes for improving the efficiency of the water splitting processes.

Acknowledgments

Ajay Kumar is thankful to the Central University of Punjab, Bathinda for providing the fellowship and research facilities. Kamlesh Yadav is grateful to the Central University of Punjab, Bathinda for providing the Research Seed Money Grant.

References

[1] Brinker C J, Hurd A J, Frye G C, Ward K J and Ashley C S 1990 Sol–gel thin film formation *J. Non-Cryst. Solids* **121** 294–302
[2] Chen C C, Nasrallah M M and Anderson H U 1993 Synthesis and characterization of $(CeO_2)_{0.8}(SmO_{1.5})_{0.2}$ thin films from polymeric precursors *J. Electrochem. Soc.* **140** 3555–60

[3] Chamberlin S E, Wang Y, Lopata K, Kaspar T C, Cohn A W, Gamelin D R and Chambers S A 2013 Optical absorption and spectral photoconductivity in α-$(Fe_{1-x}Cr_x)_2O_3$ solid-solution thin films *J. Phys.: Condens. Matter* **25** 392002

[4] Murphy A B, Barnes P R F, Randeniya L K, Plumb I C, Grey I E, Horne M D and Glasscock J A 2006 Efficiency of solar water splitting using semiconductor electrodes *Int. J. Hydrog. Energy* **31** 1999–2017

[5] Banerjee A M, Pai M R, Bhattacharya K, Tripathi A K, Kamble V S, Bharadwaj S R and Kulshreshtha S K 2008 Catalytic decomposition of sulfuric acid on mixed Cr/Fe oxide samples and its application in sulfur–iodine cycle for hydrogen production *Int. J. Hydrog. Energy* **33** 319–26

[6] Akl A A 2010 Influence of preparation conditions on the dispersion parameters of sprayed iron oxide thin films *Appl. Surf. Sci.* **256** 7496–503

[7] Yogi A and Varshney D 2013 Magnetic and structural properties of pure and Cr-doped hematite: α-$Fe_{2-x}Cr_xO_3$ ($0 \leqslant x \leqslant 1$) *J. Adv. Ceram.* **2** 360–9

[8] Wang L, Lee C Y and Schmuki P 2013 Influence of annealing temperature on photoelectrochemical water splitting of α-Fe_2O_3 films prepared by anodic deposition *Electrochim. Acta* **91** 307–13

[9] Townsend T K 2014 *Inorganic Metal Oxide Nanocrystal Photocatalysts for Solar Fuel Generation* (Berlin: Springer)

[10] Ouertani B, Ouerfelli J, Saadoun M, Ezzaouia H and Bessais B 2008 Characterisation of iron oxide thin films prepared from spray pyrolysis of iron trichloride-based aqueous solution *Thin Solid Films* **516** 8584–6

[11] Figgis B N 1966 *Introduction to Ligand Fields* (Sydney: Interscience)

[12] Lie M, Fjellvag H and Kjekshus A 2005 Growth of Fe_2O_3 thin films by atomic layer deposition *Thin Solid Films* **488** 74–81

[13] Machala L, Tucek J and Zboril R 2011 Polymorphous transformations of nanometric iron (III) oxide: a review *Chem. Mater.* **23** 3255–72

[14] Yang H, Mi W, Bai H and Cheng Y 2012 Electronic and optical properties of new multifunctional materials via half-substituted hematite: first principles calculations *RSC Adv.* **28** 10708–16

[15] Sheldon B W, Bhandari A, Bower A F, Raghavan S, Weng X and Redwing J M 2007 Steady-state tensile stresses during the growth of polycrystalline films *Acta Mater.* **55** 4973–82

[16] Hu Y S, Shwarsctein A K, Forman A J, Hazen D, Park J N and McFarland E W 2008 Pt-doped α-Fe_2O_3 thin films active for photoelectrochemical water splitting *Chem. Mater.* **20** 3803–5

[17] Duret A and Michael G 2005 Visible light-induced water oxidation on mesoscopic α-Fe_2O_3 films made by ultrasonic spray pyrolysis *J. Phys. Chem.* B **109** 17184–91

[18] Souza F L, Lopes K P, Longo E and Leite E R 2009 The influence of the film thickness of nanostructured α-Fe_2O_3 on water photooxidation *Phys. Chem. Chem. Phys.* **11** 1215–9

[19] Shwarsctein A K, Hu Y S, Forman A J, Stucky G D and McFarland E W 2008 Electrodeposition of α-Fe_2O_3 doped with Mo or Cr as photoanodes for photocatalytic water splitting *J. Phys. Chem.* C **112** 15900–7

[20] Wang Y, Lopata K, Chambers S A, Govind N and Sushko P V 2013 Optical absorption and band gap reduction in $(Fe_{1-x}Cr_x)_2O_3$ solid solutions: a first-principles study *J. Phys. Chem.* C **117** 25504–12

[21] Kaspar T C, Chamberlin S E, Bowden M E, Colby R, Shutthanandan V, Manandhar S and Chambers S A 2014 Impact of lattice mismatch and stoichiometry on the structure and bandgap of $(Fe,Cr)_2O_3$ epitaxial thin films *J. Phys.: Condens. Matter* **26** 135005

[22] Du N, Xu Y, Zhang H, Zhai C and Yang D 2010 Selective synthesis of Fe_2O_3 and Fe_3O_4 nanowires via a single precursor: a general method for metal oxide nanowires *Nanoscale Res. Lett.* **8** 1295–300

[23] Wheeler D A, Wang G, Ling Y, Yat Li and Zhang J Z 2012 Nanostructured hematite synthesis, characterization, charge carrier dynamics, and photoelectrochemical properties *Energy Environ. Sci.* **5** 6682–702

[24] Gartner M, Crisan M, Jitianu A, Scurtu R, Gavrila R, Oprea I and Zaharescu M 2003 Spectroellipsometric characterization of multilayer sol–gel Fe_2O_3 films *J. Sol–Gel Sci. Technol.* **26** 745–8

[25] Carsley J E, Ning J, Milligan W W, Hackney S A and Aifantis E C 1995 A simple, mixtures-based model for the grain size dependence of strength in nanophase metals *Nanostruct. Mater.* **5** 441–8

[26] Jain S, Adeyeye A O, Chan S Y and Boothroyd C B 2004 Interface properties of iron oxide films *J. Phys. D: Appl. Phys.* **37** 2720

[27] Goyal R N, Kaur D and Pandey A K 2009 Growth and characterization of iron oxide nanocrystalline thin films via low-cost ultrasonic spray pyrolysis *Mater. Chem. Phys.* **116** 638–44

[28] Dghoughi L, Elidrissi B, Bernede C, Addou M, Alaoui Lamrani M, Regragui M and Erguig H 2006 Physico-chemical, optical and electrochemical properties of iron oxide thin films prepared by spray pyrolysis *Appl. Surf. Sci.* **253** 1823–9

[29] Mu Q, Zhang Q, Wang H and Li Y 2012 Facile growth of vertically aligned BiOCl nanosheet arrays on conductive glass substrate with high photocatalytic properties *J. Mater. Chem.* **22** 16851–7

[30] Sivula K, Zboril R, Formal F L, Robert R, Weidenkaff A, Tucek J, Frydrych J and Grätzel M 2010 Photoelectrochemical water splitting with mesoporous hematite prepared by a solution-based colloidal approach *J. Am. Chem. Soc.* **132** 7436–44

[31] Desai J D, Pathan H M, Min S-K, Jung K-D and Joo O S 2005 FT-IR, XPS and PEC characterization of spray deposited hematite thin films *Appl. Surf. Sci.* **252** 1870–5

[32] Srinivasan G, Rajendra Kumar R T and Kumar J 2007 Li doped and undoped ZnO nanocrystalline thin films: a comparative study of structural and optical properties *J. Sol–Gel Sci. Technol.* **43** 171–7

[33] Fu D S, Suzuki H and Ishikawa K 2002 Effects of thickness on the structures and the properties of lead titantate thin films *Key Eng. Mater.* **214–15** 105–10

[34] Ashokkumar M and Muthukumaran S 2014 Modification of food ingredients by ultrasound to improve functionality: a preliminary study on a model system *Opt. Mater.* **37** 671–7

[35] Saloaro M, Majumdar S, Huhtinen H and Paturi P 2013 The effect of film thickness on the magnetic and magneto-transport properties of Sr_2FeMoO_6 thin films *EPJ Web of Conferences* **40** 15012–4

[36] Ubale A U and Belkhedkar M R 2015 Size dependent physical properties of nanostructured α-Fe_2O_3 thin films grown by successive ionic layer adsorption and reaction method for antibacterial application *J. Mater. Sci. Technol.* **31** 1–9

[37] Hankare P P, Chate P A, Sathe D J, Chavan P A and Bhuse V M 2009 Effect of thermal annealing on properties of zinc selenide thin films deposited by chemical bath deposition *J. Mater. Sci., Mater. Electron.* **20** 374–9

[38] Stokes A R and Wilson A J C 1944 A method of calculating the integral breadths of Debye–Scherrer lines: generalization to non-cubic crystals *Proc. Camb. Phil. Soc.* **40** 197–8

[39] Elias J, Zaera R T, and Clement C L 2008 Electrochemical deposition of ZnO nanowire arrays with tailored dimensions *J. Electroanal. Chem.* **621** 171–7

[40] Yadav K, Vaithyanathan V, Inbanathan S S R and Varma G D 2012 Magnetic and charge ordering properties of $Bi_{0.2}Ca_{0.8}Mn_{0.9}X_{0.1}O_3$ (where X = Ti, Cr, Fe, Co, Ni, Cu) *J. Alloys Compd.* **533** 19–24

[41] Siinde S S, Bansode R A, Bhosale C H and Rajpure K Y 2011 Physical properties of hematite α-Fe_2O_3 thin films: application to photoelectrochemical solar cells *J. Semicond.* **32** 013001
[42] Yang J, Fei L, Liu H, Liu Y, Gao M, Zhang Y and Yang L 2011 A study of structural, optical and magnetic properties of $Zn_{0.97-x}Cu_xCr_{0.03}O$ diluted magnetic semiconductors *J. Alloys Compd.* **509** 3672–6
[43] Hassan M M, Khan W, Azam A and Naqvi A H 2014 Effect of size reduction on structural and optical properties of ZnO matrix due to successive doping of Fe ions *J. Lumin.* **145** 160–6
[44] Goyal V, Bhatti K P and Chaudhary S 2010 Effect of size reduction on structural and optical properties of ZnO matrix due to successive doping of Fe ions *J. Alloys Compd.* **508** 419–25
[45] Yadav K, Singh H K and Varma G D 2012 Interplay between charge and antiferromagnetic ordering in $Bi_{0.6-x}Pr_xCa_{0.4}MnO_3$ ($0 \leqslant x \leqslant 0.6$) perovskite manganite *Physica* B **407** 1244–9
[46] Liu Y, Yu Y X and Zhang W D 2012 Photoelectrochemical properties of Ni-doped Fe_2O_3 thin films prepared by electrodeposition *Electrochim. Acta.* **59** 121–7
[47] Sharma R K and Bhatnagar M C 1999 Improvement of the oxygen gas sensitivity in doped TiO_2 thick films *Sensors Actuators* B **56** 215–9
[48] Priyadharsini P, Pradeep A, Sathyamoorthy B and Chandrasekaran G 2014 Enhanced multiferroic properties in La and Ce co-doped $BiFeO_3$ nanoparticles *J. Phys. Chem. Solids* **75** 797–802
[49] Zandi O, Beardslee J A and Hamann T 2014 Substrate dependent water splitting with ultrathin α-Fe_2O_3 electrodes *J. Phys. Chem.* C **118** 16494–503
[50] Ozer N and Tepehan F 1999 Optical and electrochemical characteristics of sol–gel deposited iron oxide films *Solar Energy Mater. Sol. cells* **56** 141–52
[51] Mallick P and Dash B N 2013 X-ray diffraction and UV–visible characterizations of α-Fe_2O_3 nanoparticles annealed at different temperature *Nanosci. Nanotechnol.* **3** 130–4
[52] Mitra S, Das S, Mandal K and Chaudhuri S 2007 Synthesis of a α-Fe_2O_3 nanocrystal in its different morphological attributes: growth mechanism, optical and magnetic properties *Nanotechnology* **18** 275608
[53] Chen Y H and Tu K J 2011 Thickness dependent on photocatalytic activity of hematite thin films *Int. J. Photon. Energy* **2012** 980595
[54] Nematollahi M, Yang X, Aas L M S and Reenaas T W 2015 Molecular beam and pulsed laser deposition of ZnS:Cr for intermediate band solar cells *Sol. Energy Mater. Sol. Cells* **141** 322–30
[55] Ali A T, Wijayantha K G U, Yarahmadi S S, Mazhar M and McKee V 2009 Nanostructured α-Fe_2O_3 thin films for photoelectrochemical hydrogen generation *Chem. Mater.* **21** 3763–72
[56] Wang Y, Muramatsu A and Sugimoto T 1998 FTIR analysis of well-defined α-Fe_2O_3 particles *Colloids Surf.* A **134** 281–97
[57] Chand P, Gaur A and Kumar A 2014 Effect of Cr and Fe doping on the structural and optical properties of ZnO nanostructures *Int. J. Chem. Nucl. Mater. Metall. Eng.* **8** 1214–7
[58] Kumar P, Rawat N, Hang D-R, Lee H-N and Kumar R 2015 Controlling band gap and refractive index in dopant-free α-Fe_2O_3 films *Electron. Mater. Lett.* **11** 13–23
[59] Bisht H, Eun H-T, Mehrtens A and Aegerter M A 1999 Comparison of spray pyrolyzed FTO, ATO and ITO coatings for flat and bent glass substrates *Thin Solid Films* **351** 109–14
[60] Mashiko H, Oshima T and Ohtomo A 2011 Band-gap narrowing in $\alpha - (Cr_xFe_{1-x})_2O_3$ solid-solution films *Appl. Phys. Lett.* **99** 241904–3
[61] Kumar S, Sharma P and Sharma V 2013 Red shift in absorption edge of $Cd_{1-x}Ni_xS$ dilute magnetic semiconductor nanofilms *J. Nanopart. Res.* **15** 1–8
[62] Kumar P and Kar M 2014 Effect of structural transition on magnetic and dielectric properties of La and Mn co-substituted $BiFeO_3$ ceramics *Mater. Chem. Phys.* **148** 968–77
[63] Kim S J, Han S H, Kim H G, Kim A Y, Kim J S and Cheon C I 2010 Multiferroic properties of Ti-doped $BiFeO_3$ ceramics *J. Korean Phys. Soc.* **56** 439–42